第 36 卷第 5 期
2017 年 10 月

红 外 与 毫 米 波 学 报
J. Infrared Millim. Waves

Vol. 36, No. 5
October, 2017

文章编号: 1001 - 9014(2017)05 - 0554 - 09

DOI:10.11972/j.issn.1001 - 9014.2017.05.008

LiDAR multichannel spectral abnormal image recognition technology for transmission lines

REN Tian-Yu[1], DUANMU Qing-Duo[1*], WU Bo-Qi[2], JIANG Hui-Lin, XU Jin-Kai, QIU Jin-Cai[3]

(1. Changchun University of Science and Technology, Changchun 130022, China;
2. Department of electrical and computer, Jilin Jianzhu University, Changchun 130000, China;
3. China Datang Technological and Economic Research Institute, Beijing 101401, China)

Abstract: The position and orientation system (POS) information of a target can be obtained through airborne laser radar (LiDAR) technology combined with the Global Positioning System, an inertial navigation system, and a laser range finder. The camera is chosen by calculating the minimum field of view resolution, pixel number, focal length, and other parameters. The LiDAR multichannel spectrum image recognition system is composed of the POS information acquisition system and the multispectral camera. The multichannel matching fusion method can produce ultraviolet, infrared, and color pictures. The elliptical shape can be fitted and parsed using the Hough transform method, the immune genetic snake model algorithm, and the least squares method, which can solve anomaly recognition problem in the insulator. The average failure detection resolution of LiDAR multi-channel spectral image anomaly recognition system is 82.4%, and it is higher than the average for copter and manual detection of 24.05%. The proposed system is a highly efficient smart grid patrol screening method.

Key words: high-voltage line inspection, LiDAR Multispectral image anomaly recognition technology, super POS information, multichannel spectral image system

PACS: 07.60.Rd, 89.20.Bb

巡线 LiDAR 多通道光谱图像异常识别技术

任天宇[1], 端木庆铎[1*], 吴博琦[2], 姜会林[1], 许金凯[1], 邱进财[3]

(1. 长春理工大学 理学院,吉林 长春 130022;
2. 吉林建筑大学 电气与计算机学院,吉林 长春 130000;
3. 中国大唐集团技术经济研究院,北京 101401)

摘要:联合 GPS、ISN、LiDAR、测距机等,构建超 POS 信息;计算最小视场分辨率、像元数、焦距等选择相机;将 POS 采集系统与相机组合成 LiDAR 多通道光谱图像异常识别系统. 采用多通道匹配融合法融合紫、红外、彩色图片,基于 Hough 变换,通过同族容器归纳法确定疑似故障点. 运用 Hough 变换、免疫遗传 Snake、最小二乘法解析椭圆形貌,解决绝缘子异常识别问题. 工程实验表明,该系统平均探测精度是 82.4%,优于直升机与人工平均值 24.05%,是一种高效率的智能电网巡线排查手段.

关 键 词:输电线路巡检;激光雷达多光谱图像异常识别;超 POS 信息;多通道光谱成像系统

中图分类号:TP7,V27 **文献标识码**:A

Introduction

The maintenance of grid security and stability, as well as the efficient operation of transmission line inspection, are particularly important because of the need to modernize pipe network construction. Transmission lines exhibit interregional distribution and multifaceted points; they are also installed in a complex terrain where the natural environment is poor. Continuous mechanical tension, lightning strikes, material aging, icing, and human factors result in inverted towers, broken

Received date: 2017-01-20, **revised date**: 2017-07-20 **收稿日期**:2017-01-20, **修回日期**:2017-07-20

Foundation items: Supported by Jilin Key Science and Technology Research Fund (130202GX010012794); National Natural Science Foundation of China (61077024, 11474037); Specialized Research Fund for the Doctoral Program of Higher Education of China (20112216120005)

Biography: REN Tian-Yu (1983-), male, Jilin, Ph. D. Research area involves spectral sensors and development of UAV system. E-mail: ceo@uslsolutions.com

* **Corresponding author**: E-mail: duanmu@cust.edu.cn

stocks, wear, corrosion, dancing, and other phenomena. Insulators are also damaged by lightning, while tree growth caused by high-pressure oil discharge, insulation degradation, and other issues can easily lead to transmission line accidents, tower theft, and other incidents[1]. These circumstances must be promptly addressed and repaired.

At present, traditional patrol inspection adopts the traditional artificial inspection and navigation patrol lines. (1) The traditional manual inspection line method is highly dangerous, difficult, time-consuming, costly, and exhibits low resolution. Artificial methods must be applied to patrol lines because of complex line section inspection items. The minimum target resolution is over 40 mm, and more than 50% of the blind area is covered[2]. (2) The navigation patrol line is divided into the manned aircraft patrol line and the unmanned robot operations. Manned aircraft patrol line operations that utilize helicopters currently handle power systems under the traditional method. Unmanned aerial vehicle (UAV) driving patrol line operations that commonly use online robots and UAVs in line work comprise a popular subject in national engineering staff research. At this stage, the remote imaging resolution of the navigation patrol method is over 15 mm and its hovering resolution is more than 10 mm. With the continuous development of the computer vision industry, the use of helicopters to inspect transmission lines can automatically generate line defect reports and maintenance programs, which are gradually replacing manual operations[3-5].

The insulator, which is an important component of an air transmission line, can withstand tremendous mechanical tension and high voltage. A transmission line significantly affects security. The detection of insulator anomaly by using a camera to obtain an image and data information of an insulator is an important method that can determine the contamination quantity, burst degree, and defect degree of the insulator. Ge Yu-min et al. (2010) proposed a detection algorithm for the number of insulators to achieve fault detection; this algorithm could be adopted in aerial helicopter intelligent inspection systems[6]. Fang Ting of the Anhui University of Technology (2013) and Kailasam Saranya of the KSR University in India (2016) reported a new fault detection algorithm based on insulator characteristics and shape. These researchers utilized the immune genetic snake algorithm, synchronous phasor estimation, PMU, vector machine classification, and other methods to establish a dynamic model and generate the geographical region of an insulator. Under normal conditions, an algorithm that can detect an insulator in a line every 0.5 s is the most important factor[8]. An accuracy level of 92% can be applied effectively in unmanned aerial vehicle (UAV) detection[9]. The insulator detection algorithm and the practical application of high-performance methods still require considerable research.

The current study presents a LiDAR multispectral image anomaly detection technology to overcome and improve the shortcomings of existing navigation inspection methods and algorithms. The proposed anomaly detection technology is aided by a UAV patrol method that can attain high efficiency, high speed, and high accuracy of airborne transmission line patrol through its recognition technology and implementation system. The LiDAR multispectral image recognition technology aims to realize the minimum resolution and stability of a system. This technology was developed by optimizing the geographic location acquisition and multi-spectral image acquisition device. It can apply image information to effectively detect abnormality in a transmission line and focus on solving the contour and shape of an insulator, as well as on identifying and detecting its characteristics. The aforementioned system is applied to the inspection process of transmission lines. Considerable data show that recognition technology significantly improves work efficiency and accuracy.

1　LiDAR and multichannel spectral image system

Transmission line inspection is achieved by acquiring aerial information and aerial survey information, such as POS aerial photos and photos collected from the LiDAR multi-channel spectral image anomaly recognition system (Fig. 1). This system is composed of a geographical location (POS) information acquisition system and a multi-spectral camera on a pod. The camera comprises ultraviolet (UV), infrared (IR), and color cameras, which are used to collect an image in three bands (UV, IR, and visible light). The location information acquisition system adopts the Global Positioning System (GPS)/inertial navigation system (INS), LiDAR, and an inclination sensor to collect POS information. The two types of data collected by the system are merged via multi-channel matching and then processed through image recognition, homogeneous container induction, and anomaly recognition. Finally, the corresponding picture information can be obtained at different positions to determine whether the transmission line is intact or abnormal. This paper put forward using strap down inertia and INS positioning difference way to shoot area specific image difference, as well as realizing the consistency of induction for the different directions and parameters images with polygon location rules.

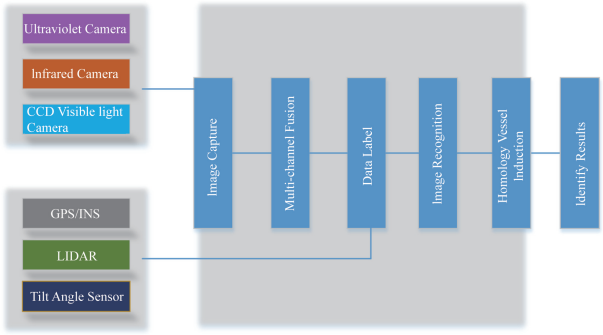

Fig. 1　LiDAR abnormal image recognition system
图 1　LiDAR 多通道光谱图像异常识别系统

1.1　Super POS information acquisition system

The super POS information acquisition system (Fig. 2) is composed of LiDAR, GPS, an Apresys TP2000 laser range finder, an INS, and an ADS40 digit-

al aerial camera. This system establishes a database table and provides air position information.

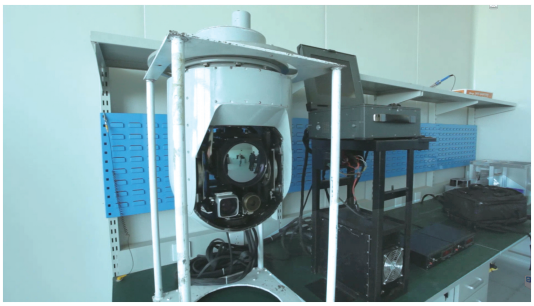

Fig. 2 POS information acquisition system
图2 POS信息采集系统

LiDAR provides the echo energy with the pitch angle and height information of target to the detected platform, which operating principle is shown in Fig. 3. A ground GPS base station and an aircraft mobile station are used for dynamic GPS synchronization measurement. The coordinates of the aircraft mobile station are obtained based on the coordinates of the base station. Therefore, the accuracy of the coordinates of the reference station directly affects the accuracy of the coordinates of the aircraft mobile station. The known GPS coordinates cannot be used as the base station under normal conditions due to constraints in traffic, communication, power supply, satellite elevation angle, electromagnetic wave interference, and multi-path effect. Hence, the base station must exhibit highly accurate measurement and calculation work. The airport and aerial survey area has one base station each. If the survey area is large, then it can be set on two to three compasses and GPS base stations. The compass and GPS base station for POS information provide the WGS84 coordinates and airborne Beidou positioning difference to determine the transmission line, identify the abnormal target, and provide accurate target location.

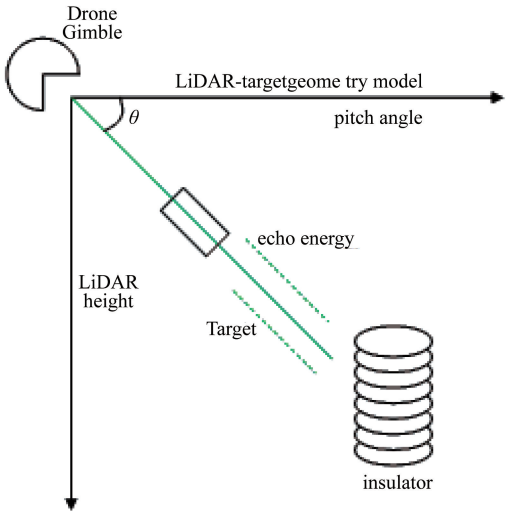

Fig. 3 LiDAR operating principle
图3 激光雷达工作原理

1.2 Visible light system

The visible light system is based on a CCD detector. The minimum resolution β_{MIN} of the 60 m target of the visible light system must be smaller than 2mm (i. e., $\beta_{MIN} < 2$ mm). Target imaging on the CCD detector accounts for more than 1 pixel, and the CCD pixel resolution ΔL is 2 mm. From the observation distance L, the pixel angular resolution α is obtained as follows:

$$\alpha = \Delta L/L = 25\ \mu\text{rad} \quad . \quad (1)$$

Equation 1 is the minimum field resolution. β_{MIN} and α are utilized as functions of the minimum pixel number to find the camera N as follows:

$$N = \beta_{MIN}/\alpha = 1\ 200 \quad . \quad (2)$$

The CCD optical system must exhibit high sensitivity to reduce exposure time, which requires maximum CCD sensor pixel size to achieve electronic debounce. Under an instantaneous field angle, a large CCD will increase the focal length of the optical system, thereby resulting in difficulties in miniaturizing system structure. Weight increase decreases system control quality. These factors are considered in selecting Imperx IGV-B2630C camera (USA), the main performance indicators of which are listed in Table 1. The system performance of the camera satisfies operational accuracy requirements.

Table 1 IGV-B2630CMain performance indicators
表1 IGV-B2630C 主要技术参数

Indicator	Performance
Resolution	4 600×3 200
Shutter speed	1/100000-1/35 s
Camera interface	GigE
Effective imaging area	11.84 m×8.88 mm
Minimum illumination	1.0 Lux
Pixel size	7.4 μm×7.4 μm
FPS	44 fps
DCLK	50 MHz
SNR	60 dB

The visible light filter is removed, and the band-pass cutoff filter is added according to the system parameters and the high-resolution CCD sensor. The IGV-B2630C camera can then obtain 280 ~ 470 nm (UV) and 900 ~ 1200 nm (IR) images within the image information. The relationship between the maximum focal length f_1 and pixel size A of the optical system[10] is calculated as follows to ensure that pixel angular resolution α is over 25 μrad:

$$\alpha = A/f_1 \quad . \quad (3)$$

Thus, f_1 is 296 mm, which is rounded off to 300 mm. When the optical system is in the maximum field of view,

$$Tg(\beta_{MAX}/2) = C/2f_2 \quad , \quad (4)$$

where C is the effective pixel area of the diagonal length. The IGV-B2630C camera is 14.8 mm, and thus, the obtained f_2 is 74 mm. On the basis of the f_1 and f_2 values, the optical system has 5 × zoom capability. When the relative aperture is considered, the optical system diameter D is set to Φ50 mm. Hence, the minimum target of 3 mm can be resolved at 60 m.

The camera was placed in a car (Fig. 4). The working mechanism is described as follows: the object detected by light enters the optical system, passes through the sensor, and into the photoelectric detection

system. The detector then forms an original picture. The multispectral imaging system consists of visible, UV, and IR coaxial cameras. The multispectral image is formed via multi-channel image fusion technology. This technology and the image treatment method are explained in detail in the following section.

(a)　(b)

Fig. 4　Multi-spectral camera on a pod: (a) multi-spectral camera and controlling system and (b) diagram of the airborne camera
图 4　吊舱内多光谱相机(a)多光谱相机与控制系统(b)机载相机实物图

2　Abnormal image recognition technology

The LiDAR multi-channel spectral image anomaly recognition system measures the position and the image. It uses image anomaly recognition technology to deal with two aspects of the data. As shown in Fig. 1, data processing is mainly divided into multi-channel matching fusion, image recognition, same group container induction, and anomaly recognition.

2.1　Image preprocessing

2.1.1　Multi-channel matching fusion

The image fusion of the UV, IR, and color multi-channel information is accomplished using the homogeneous container induction method based on super POS information. This method uses a high-resolution image from the visible light region as the base sample. It then compares the non-container image in adaptive learning mode by superimposing the channel information of the thermal imaging channel and the information of the UV image. Therefore, this process is a multi-channel matching and fusion method.

LiDAR triggers the system to automatically take pictures and videos of the key targets by using smart camera identification and onboard computer intelligent filtering, eg Fig. 5. The time interval shift transforms the key frame for the stored photo samples. AUM is used to evaluate function variance and uncorrected function. The multi-channel image sample is stored at a particular time when the frame-frequency image in the judgment interval cannot be focused on. The quadratic function fitting method is adopted to obtain the fitting curve of the discrete points, and the highest point of the curve is the optimal focusing position. Potential errors exist in autofocus. The error of the response curve is compensated using LiDAR multi-point ranging and quadratic function fitting methods. The bidirectional transformation of the visible light camera and IR movement is then realized. Function comparison is conducted to further reduce possible errors. The conditional constraint of air information adopts the precise ranging constraint method. It also uses a small-scale and accurate target screening method for the same-frame image, and provides early check ability for the subsequent image processing of data.

The current POS aerial mode utilizes geographical location photography. Research on POS photography technology initially presented a type of super POS image photography. The original POS data accurately superpose target distance information. Angle information summarizes the container with a robust characteristic. This super POS photography image acquisition mechanism is automatically classified as a kin container. An inductive system for each stored photo adopts a 3D data storage method. This method labels pictures with tags that indicate GPS information, tag information, location, angle, and matching pictures. The super POS information for the kin container sums up the data to be processed to provide a domain range. This range uses POS data processing with the method for classifying kin images at different times, shooting angles, and positions of discrete images. Tag information is stored in the form of text labels in a table text database for fast application. The links are embedded via onboard computer virtualization implementation in BSD environment. The table records of the air current camera coordinate system points a gathering pace into the target distance by LiDAR. An angle sensor measures the angle and accurate location information for a fast detection area. The kin container information provides accurate calibration by using fixed target shooting and the difference after the precise distance. When computer processing generates different photos, the air position information acquisition system can be effective for elements with different imaging angles and fine images provided by the kin container to eliminate the different architecture of repeated repository images. Unlike advanced image frame interval detection methods, kin container induction, which is a pioneer in air parameter, geographic coordinate, and pitch detection methods, is powerful and avoids repetition of the same category pictures, regression, and blindness.

The same family of containers is not a simple summary of the fusion of image data and POS information. The pictures are individually processed to achieve fine and accurate classification under different conditions. In the process of computing data that cannot be measured, the nonlinear separability of sample space must be solved into a linear separable problem in feature space and a wide area to realize a high-precision target with a small space and fast processing speed. The data are processed via the Hough transform method after multi-spectral multi-channel camera target image acquisition, LiDAR ranging, and contour recognition.

Hough transform is a parameter estimation principle that uses voting technology[11-13]. Its principle is to use image space and the Hough parameter space point (line duality theorem) in the detection problems of image space transformation into parameter space using accumulative statistics in parameter space. The Hough peak method is then applied to detect linear parameter space and find an accumulator. This transformation type exhibits a relationship between the image space of pixels and clustering, which can be identified in analytical form by linking parameter space to corresponding points. The transformation has an ideal effect on parameter space un-

der maximum 2D condition. On the basis of Hough change, the support vector machine (SVM) method[14-16] is introduced into nonlinear mapping, which maps 2D space onto high-dimensional (or infinite dimensional) feature space in Hilbert space. Thus, calculation efficiency is improved.

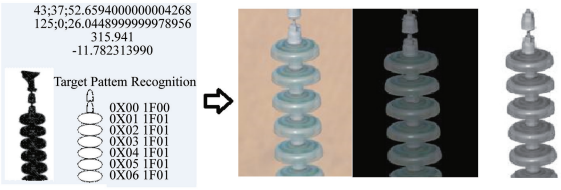

Fig. 5 Image processing
图5 图像处理过程

A real topological space of a transmission line can be constructed to immediately recognize the abnormality of an image based on improving the processing efficiency of image and POS information. An Apresys TP2000 laser range finder points to the target area of the central area range and feedback angle. It is combined with a UAV flight control that cites a lead number to the absolute accuracy of the target and the location. The picture is assumed to be the same target of a different spatial point, and the appearances of different azimuth angles are collected when shooting at another angle, and when the elevation and position points overlap in the WGS84 coordinate. The spatial topological method used in this study is a continuous-type fuzzy topological linear space, which realizes the correlation of the spatial domain. The aforementioned analysis can preprocess images, and thus, can be regarded as an abnormal image recognition method.

The insulator is an important part of a transmission line; consequently, this study focuses on the morphological feature recognition algorithm.

2.2 Insulator abnormal recognition

2.2.1 Hough transform

The main feature of an insulator is a linear elliptical string, and many sagging areas exist in the boundary. An effective algorithm can detect the ellipse via Hough transform. The ellipse is described by five parameters: the center of the ellipse, the major axis, the minor axis, and the angle between the long and short axes (Fig. 6).

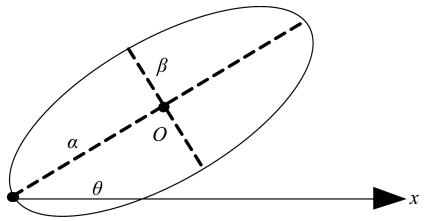

Fig. 6 Ellipse and its parameters
图6 椭圆参数标定

Any point on the elliptic boundary satisfies the following equation:

$$\frac{(x-x_0)^2}{a^2}+\frac{(y-y_0)^2}{b^2} \quad . \quad (5)$$

The derivative of Eq. 5 is obtained using the direction information of the boundary by computing three independent parameters: a, b, and ξ. These three parameters determine the center of the ellipse (x_0, y_0). Among these parameters, $\xi = \frac{\mathrm{d}(y-y_0)}{\mathrm{d}x}$. When $\theta \neq 0$, $\xi = \tan\left(\varphi - \theta - \frac{\pi}{2}\right)$. The tangential orthogonal solution φ is obtained at the edge point (x, y). The edge will be analyzed, and thus, the elliptic θ in quantitative values can be obtained as ξ.

Point O is the center of the oval, and its position is (o_x, o_y). α and β are each defined as the length of the long and short axes of the oval. The angle of the long and x axes is also defined as θ. Thus, we can obtain the ideal oval when the five parameters are known $\{o_x, o_y, \alpha, \beta, \theta\}$. In Fig. 7, the short axis is defined as $l_{r,s}$ and the long axis is defined as $l_{t,u}$, where r and s are two endpoints of the short axis, whereas t and u are two endpoints of the long axis. When endpoints t and u are assumed as the edge points of the oval in the image, we can calculate the four remaining parameters $\{o_x, o_y, \alpha, \theta\}$ using (t_x, t_y) and (u_x, u_y). In this case, only the length β of the short axis of the oval can be obtained by using the remaining elliptical edge points to determine parameter β. Only parameter β is determined; thus, only 1D accumulator space is required. This method is the oval detection algorithm based on the 1D Hough exchange space.

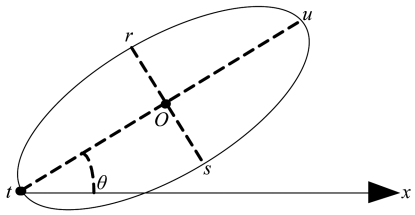

Fig. 7 Ellipse in the Hough algorithm
图7 Hough 变换的椭圆算法

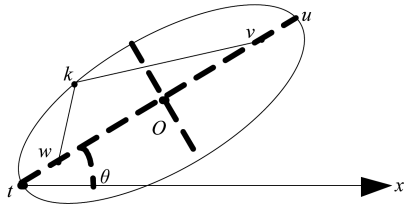

Fig. 8 Ellipse with the focal length in the Hough algorithm
图8 Hough 变换的带焦距的椭圆算法

Figure 8 shows a diagram of the oval with the focal length, where w and v are two focal points of the oval. When the fix points (t_x, t_y) and (u_x, u_y) are given, we can then calculate $\{o_x, o_y, \alpha, \theta\}$ as follows:

$$o_x = \frac{t_x + u_x}{2}, o_y = \frac{t_y + u_y}{2} \quad , \quad (6)$$

$$\alpha = \frac{\sqrt{(u_x - t_x)^2 + (u_y - t_y)^2}}{2} \quad , \quad (7)$$

$$\theta = \tan^{-1}\left(\frac{u_y - t_y}{u_x - t_x}\right) \quad , \quad (8)$$

$$\sqrt{(k_y - w_y)^2 + (k_x - w_x)^2} + \sqrt{(k_y - v_y)^2 + (k_x - v_x)^2} = 2\alpha \quad . \quad (9)$$

Furthermore,

$$w_x = o_x - \cos|\theta|\sqrt{\alpha^2 - \beta^2} \quad , \quad (10)$$

$$w_y = o_y - \sin|\theta|\sqrt{\alpha^2 - \beta^2} \quad , \quad (11)$$

$$v_x = o_x + \cos|\theta|\sqrt{\alpha^2 - \beta^2} \quad , \quad (12)$$

$$v_y = o_y + \sin|\theta|\sqrt{\alpha^2 - \beta^2} \quad . \quad (13)$$

For a given ellipse on the contour of any point k, the β value can be determined using Eqs. 10-11. Thus,

$$\beta = \sqrt{\frac{\alpha^2\delta^2 - \alpha^2\gamma^2}{\alpha^2 - \gamma^2}} \quad , \quad (14)$$

such that

$$\delta = \sqrt{(k_y - o_y)^2 + (k_x - o_x)^2} \quad , \quad (15)$$

$$\gamma = \sin|\theta|(k_y - o_y) + \cos|\theta|(k_x - o_x) \quad . \quad (16)$$

2.2.2 Immune genetic algorithm snake model

Contour extraction is attained by combining the immune genetic snake model algorithm[17-18] with the Hough transform. The energy function of the snake model is used as the objective function, which is expressed as follows:

$$E_{\text{snake}} = \int_0^1 [E_{\text{int}}(v(s)) + E_{\text{ext}}(v(s))]\,\mathrm{d}s \quad , \quad (17)$$

where E_{int} is the main area after the LiDAR to determine the strength of the insulator outline signal, $E_{\max}$ is the LiDAR that determines the main image signal intensity outside the area and does not contain an insulator profile, and $E_{\max} = -\nabla|I(x,y)|^2$. The external binding is the LiDAR point cloud contour filtering process.

2.2.3 Least squares ellipse fitting method

The insulator cross-point detection template is constructed after filtering the contour background using Hough transform and the immune genetic snake model algorithm. As shown in Fig. 9, the different insulator cross-point detection templates are divided into six types in 5 × 5 pixel regions. The cross-point image matching detection is sequentially performed on the edge image after morphological processing.

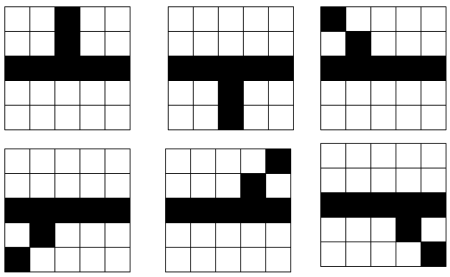

Fig. 9　Detection template structure of the insulator intersection

图 9　绝缘子交叉点检测模板结构图

Ellipse fitting is performed by using the direct least squares[19] ellipse fitting method according to the intersection points of the edge points in the insulator disk area (Fig. 10). The position of the original image shows the fitted ellipse, where each ellipse corresponds to a disk surface of the insulator. A method that extracts the single disk surface of the insulator in the visible light image of the transmission line is then realized.

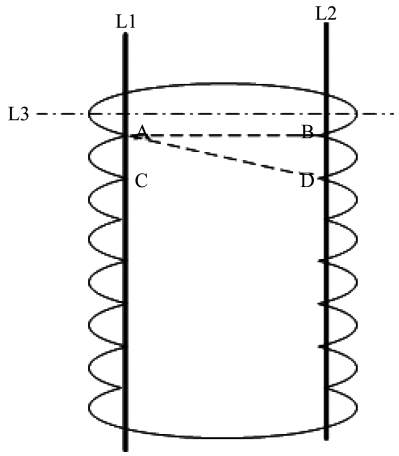

Fig. 10　Structure of the insulator

图 10　绝缘子盘面结构

The definition of the ellipse center is (x_0, y_0) for the angle of rotation and the axial direction, respectively (a, b). The assumptions, $n(x,y), m(x,y_i)$ exist on the edge and ellipse points, respectively, with three points on a straight line. The edge points with an elliptical point for the geometric distance are expressed as follows:

$$\Delta r = \sqrt{(x - x_0)^2 + (y - y_0)^2} - \sqrt{(x_i - x_0)^2 + (y_i - y_0)^2} \quad . \quad (18)$$

The best fitting is the edge of the geometric distance of the ellipse, which is the minimum sum of the squares. The objective function is zero. Thus,

$$k = \sum_{i=1}^{n} \left(\sqrt{(x - x_0)^2 + (y - y_0)^2} - \sqrt{(x_i - x_0)^2 + (y_i - y_0)^2}\right)^2 \quad . \quad (19)$$

The five parameters of the ellipse are substituted into the equation to obtain the most fitting ellipse information, and the contours of the insulator are extracted from the ellipse. Through the above algorithm processing, the insulator can be displayed in Fig. 5. Based on the above image processing, we developed a novel assistant program and interface (Fig. 11).

Fig. 11　Novel assistant program and interface

图 11　匹配辅助程序与界面

3　Experiments and analyses

The LiDAR multi-spectral anomaly recognition sys-

tem and technology is applied to an actual project. The working status of the system is shown in Fig. 12, which will be the transmission line in the different examples for the experiments and analyses.

(a) (b)

Fig. 12 Operative modes of the LiDAR abnormal multi-channel spectral image recognition system: (a) first mode and (b) second mode

图 12 LiDAR 多通道光谱图像异常识别系统工作状态(a)工作状态 1(b)工作状态 2

3.1 Insulator defect contour extraction and recognition

Insulators frequently exhibit three types of defects in abnormal conditions in engineering applications, as shown in Fig. 13. SVM and Hough transform are implemented with pattern recognition in the process of insulator defect. Figures 15(a) and 16(a) show images obtained using a white-light camera, whereas Figs. 16(b) and 16(b) show images obtained using an IR camera. Figures 15 and 16 present two examples of acquisition using the proposed system. Figures 15(d), 15(d), and Fig. 13 show the recognition of the key components using LiDAR.

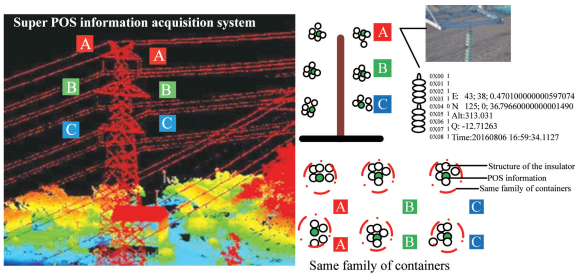

Fig. 13 SVM and Hough transform are implemented with pattern recognition in the process of insulator defect

图 13 用于绝缘子异常探测处理的 SVM 与 Hough 变换过程

(a) (b) (c)

Fig. 14 Abnormal insulator: (a) damage in the umbrella skirt of composite insulators, (b) explosive insulator, and (c) burns on the insulator surface

图 14 绝缘子缺损异常(a)复合绝缘子伞裙破损(b)绝缘子自爆(c)绝缘子釉表面灼伤

3.2 Hidden discharge point extraction and processing

The outline of the measured object in the multi-spectral mode is recognized using LiDAR. The outer surface of the measured object is also photographed through the UV spectral band. After the combination of visible and IR images, SVM robustness processing is conducted to obtain the key feature points, i. e., to determine the points of failure. Figure 18(a) show images obtained using a white-light camera, whereas Fig. 17(b) show images obtained using an IR camera. Figures 17(b) and 18(b) show two examples of acquisition using the proposed system. Figures 17(c), 18(c), and Figs. 17(d), 18(d) show the recognition of the post-recognition contour.

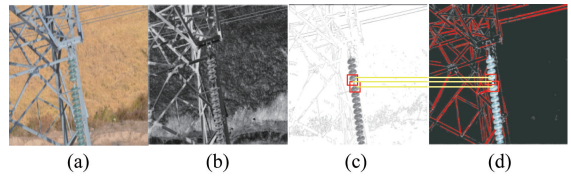

(a) (b) (c) (d)

Fig. 15 First example of the extraction and recognition of intelligent insulator defects

图 15 绝缘子缺损轮廓提取与识别事例一

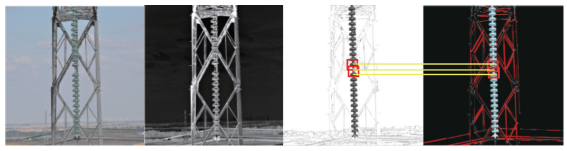

(a) (b) (c) (d)

Fig. 16 Second example of the extraction and recognition of intelligent insulator defects

图 16 绝缘子缺损轮廓提取与识别事例二

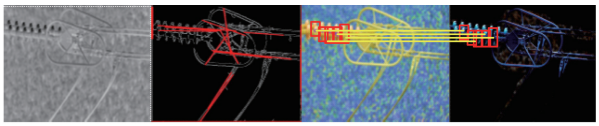

(a) white-light camera (b) LiDAR data (c) multispectral camera (d) recognize and output

Fig. 17 First example of the extraction and recognition of the hidden discharge point

图 17 隐蔽放电点的提取与识别事例一

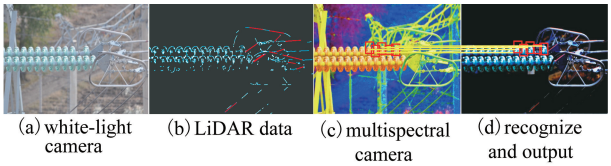

(a) white-light camera (b) LiDAR data (c) multispectral camera (d) recognize and output

Fig. 18 Second example of the extraction and recognition of the hidden discharge point

图 18 隐蔽放电点的提取与识别事例二

PEIPORT of Hong Kong currently utilizes the other side of the failure point of the technology to obtain the highest accuracy. The minimum target recognition degree of 50 mm is shown in Fig. 19(a). The developed system has a minimum target recognition degree of 3 mm, which is higher than the domestic and international levels. For this reason arithmetic adopt Hough transform, recognition

by Kalman filter and computer nerve network. So, it can only recognize electrically insulates contacts, arc discharging scar, shock hammer, wires those model. For the others it need more continue in-depth studies. we should develop more function of the product and make it more perfect in the future. The aforementioned examples show that the LiDAR multi-spectral image anomaly recognition technology has been fully applied and practiced in real engineering, and its practical application value and significance have been demonstrated.

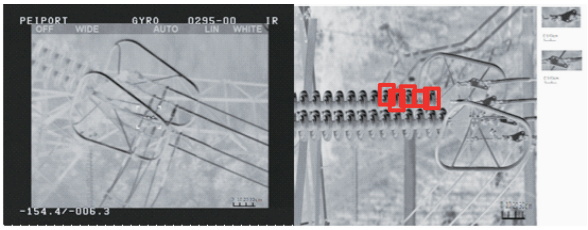

(a) only video record　(b) LiDAR multi-spectral image anomaly recognition

Fig. 19　Comparison of the minimum target identify degrees: (a) from Hong Kong PEIPORT and (b) from the LiDAR multi-channel spectral abnormal image recognition system
图 19　最小目标识别效率对比(a)香港 PEIPORT 彼岸科技(b)LiDAR 多通道光谱图像识别系统

This paper demonstrates failure detection accuracy about three ways, which include manual detection, copter detection and LiDAR multi-channel spectral image anomaly recognition system, through taking an example of Tiansong section of electric power transmission line. The detected section is located between Baicheng and Songyuan city in Jilin province, China, its total length is about 200 km. The statistic data is shown in Table 2. Songtian section is recorded as ST.

The average failure detection accuracy of copter detection $\varepsilon_{\text{copter}}$ is calculated as

$$\varepsilon_{\text{copter}} = \frac{N_{\text{copter}}}{N_{\text{all}}} = 66.7\% \quad . \quad (20)$$

While the average failure detection accuracy of manual detection $\varepsilon_{\text{manual}}$ is achieved by

$$\varepsilon_{\text{manual}} = \frac{N_{\text{manual}}}{N_{\text{all}}} = 50\% \quad . \quad (21)$$

Hence, the average for $\varepsilon_{\text{copter}}$ and $\varepsilon_{\text{manual}}$ is shown as

$$\bar{\varepsilon} = \frac{1}{2}\left(\frac{N_{\text{copter}}}{N_{\text{all}}} + \frac{N_{\text{manual}}}{N_{\text{all}}}\right) \quad , \quad (22)$$

and the average failure detection accuracy of LiDAR multi-channel spectral image anomaly recognition system is gained as

$$\varepsilon_{\text{uav}} = \frac{N_{\text{UAV}}}{N_{\text{all}}} = 82.4\% \quad . \quad (23)$$

So using the novel method, the failure detection accuracy is improved to

$$E = \varepsilon_{\text{uav}} - \bar{\varepsilon} = \frac{N_{\text{UAV}}}{N_{\text{all}}} - \frac{1}{2}\left(\frac{N_{\text{manual}}}{N_{\text{all}}} + \frac{N_{\text{copter}}}{N_{\text{all}}}\right) = 24.05\% \quad . \quad (24)$$

The failure detection accuracy of LiDAR multi-channel spectral image anomaly recognition system is the highest, and it is obviously to find that its accuracy value can last for the longset time among the three methods.

4　Conclusion

This study proposes a LiDAR and POS multi-channel spectral image recognition technique to realize the engineering purpose of airborne power transmission line patrol. The multi-spectral images of ultra-POS multi-channel UV, IR, and visible light detectors are calculated and analyzed. The super POS information of the LiDAR, GPS, Beidou, and INS hybrid differential mode position information acquisition systems is introduced. The automatic recognition of the insulator defect anomaly in a complex background is realized, and the accuracy of picture information is ensured. The proposed algorithm uses the multi-channel processing comparison method, the same family container induction method, and the boundary detection algorithm of organic fusion. The multi-channel acquisition images are pattern recognition and numerical calculation, which is complex background insulator multi-disk information extraction method. Theory and design research in engineering practice show that the minimum identification degree of the system is 3 mm, which is higher than those of existing local and international technologies. The utilization efficiency is also considerably higher than the expected result and the values for artificial identification and general aviation helicopter/UAV efficiency. The LiDAR multi-spectral image anomaly recognition technology for inspecting airborne power transmission lines exhibits high efficiency, precision, and application value.

References

[1] Siroma Z, Fujiwara N, Yamazaki S, *et al*. Mathematical solutions of comprehensive variations of a transmission-line model of the theoretical

Table 2　Detected data
表 2　巡线探测数据表

	Name	Mode	Days	Peoples	Period	Tower	Review	Torsional damper	Spacer	Insulator	other	total
1	ST1/2	manual	30	32	10	400	2	51	23	304	69	447
2	ST1/2	copter	20	6	20	397	1	23	17	274	47	361
3	ST1	copter	180	12	30	520	3	65	43	397	67	572
4	ST 1	LiDAR	4	3	0	100	0	6	5	19	12	42
5	ST 1	copter	3	4	1	100	0	2	2	13	7	34
6	ST 1	manual	10	4	0	100	0	3	2	12	8	25
7	ST 1	manual	30	12	5	100	3	6	5	18	22	51
8	ST 1	Later period	10	5	100	0	6	5	19	22	51	

impedance of porous electrodes[J]. *Electrochimica Acta*, 2015, 160: 313-322.
[2] WANG Bo, WU Gong-ping, XU Chang-ming, *et al*. Research and development of backstage management and inspection system based on transmission line inspection robot[J]. *Engineering Journal of Wuhan University*(王波,吴功平,许昌明,等. 输电线路巡检机器人后台管理及诊断系统. **武汉大学学报**: 工学版), 2014, **47**(1): 110-114.
[3] ZHAO Yu, WANG Xian-pei, HU Hong-hong, *et al*. Early Warning for Various Internet Faults of GIS Based on Ultraviolet Spectroscopy [J]. *Spectroscopy and Spectral*(赵宇,王先陪,胡红红,等. 基于紫外光谱检测的 GIS 内多类故障早期预警, **光谱学与光谱分析**), 2015:02-15.
[4] FANG Ting, DONG Chong, HU Xing-liu, *et al*. Contour Extraction and Fault Detection of Insulator Strings in Aerial Images[J]. *Journal of shanghai jiaotong university*(方挺, 董冲,胡兴柳,等. 航拍图像中绝缘子串的轮廓提取和故障检测. **上海交通大学学报**), 2013(12).
[5] GE Yu-min, LI Bao-shu, ZHAO Shu-tao, *et al*. A method based on aerial images to detect the surface state of insulators[J]. *High Voltage Apparatus*(葛玉敏,李宝树,赵书涛,等. 基于航拍图像的绝缘子表面状态检测. **高压电器**), 2010(04).
[6] Kyrchanova O, Mogila V, Wolle D, *et al*. Functional Dissection of the Blocking and Bypass Activities of the Fab-8 Boundary in the Drosophila Bithorax Complex[J]. *PLoS Genet*, 2016, **12**(7): e1006188.
[7] GE Yu-min, LI Bao-shu, LIANG Shuang. A method based on aerial images to detect the surface state of insulators[J]. High Voltage Apparatus(葛玉敏,李宝树,梁爽. 数学形态学在绝缘子图像边缘检测中的应用. **高压电器**), 2012, **48**(1): 101-104.
[8] FANG Ting, DONG Chong, HU Xing-liu, *et al*. Counter extraction and fault detection of insulator strings in aerial images[J]. *Journal of Shanghai Jiaotong university*(方挺, 董冲,胡兴柳,等. 航拍图像中绝缘子串的轮廓提取和故障检测. **上海交通大学学报**), 2013, **47**(012): 1818-1822.
[9] Saranya K, Muniraj C. A SVM Based Condition Monitoring of Transmission Line Insulators Using PMU for Smart Grid Environment[J]. *Journal of Power and Energy Engineering*, 2016, **4**(03): 47.
[10] Zhai Y, Wang D, Zhang M, *et al*. Fault detection of insulator based on saliency and adaptive morphology[J]. *Multimedia Tools and Applications*, 2016: 1-14.
[11] WU Yi-nan, LI Guo-ning, ZHANG Ning. Calculation of overlapping pixels in interleaving assembly for CCD focal plane of space camera [J]. *Optics and Precision Engineering*(武奕楠,李国宁,张宇. 空间相机焦平面 CCD 交错拼接重叠像元数计算. **光学精密工程**), 2016, **24**(2): 422-429.
[12] Kyrchanova O V, Leman D V, Toshchakov S V, *et al*. Induction of transcription through the scs insulator leads to abnormal development of Drosophila melanogaster[J]. *Russian Journal of Genetics*, 2016, **52**(10):1007-1014.
[13] Kyrchanova O, Mogila V, Wolle D, *et al*. Functional Dissection of the Blocking and Bypass Activities of the Fab-8 Boundary in the Drosophila Bithorax Complex[J]. *PLoS Genet*, 2016, **12**(7): e1006188.
[14] Avva S V S P. Characterization of Boundary Element-Associated Factors BEAF-32A and BEAF-32B and Identification of Novel Interaction Partners in Drosophila Melanogaster[D]. Faculty of the Louisiana State University and Agricultural and Mechanical College in partial fulfillment of the requirements for the degree of Doctor of Philosophy in The Department of Biological Sciences by SV Satya Prakash Avva B. Tech., ICFAI University, 2016.
[15] Sadeghi L. Modulating chromatin by transcription and nucleosome turnover: a genome-wide study in fission yeast [M]. Inst förbiovetenskaperochn ringsl ra/Dept of Biosciences and Nutrition, 2015.
[16] Sadeghi L. Modulating chromatin by transcription and nucleosome turnover: a genome-wide study in fission yeast[J]. 2015.
[17] Griffin D K, Fowler K E, Peter J, *et al*. 20th International Chromosome Conference (ICCXX)[J]. *Chromosome Research*, 2015, **23**(2): 343.
[18] Sunagar K, Jackson T N W, Undheim E A B, *et al*. Three-fingered RAVERs: rapid accumulation of variations in exposed residues of snake venom toxins[J]. *Toxins*, 2013, **5**(11): 2172-2208.
[19] Wu Y, Wang Y, Jia Y. Segmentation of the left ventricle in cardiac cine MRI using a shape-constrained snake model[J]. *Computer Vision and Image Understanding*, 2013, **117**(9):990-1003.
[20] WANG Le-yang, XU Cai-jun. Voxels and the construction of a virtual geographic environment[J]. *Geomatics and information science of Wuhan univetsity*(王乐洋, 许才军. 总体最小二乘研究进展 **武汉大学学报**: 信息科学版), 2013, **38**(7): 850-856.

(上接第 553 页)

cell model without skin effect. The deviation is 2% for S_{11}, 3% for S_{12}, 1.5% for S_{21} and 4% for S_{22}.

4 Conclusion

An improved small-signal model for nanometer MOSFET device is developed in this paper. The better result is achieved by modeling the MOSFET with multiple cells considering skin effect of feedlines. It is more desirable to take the effect of interconnection between elementary cells into account. According to the parameters of the conventional one cell model, physically expected results are obtained for the parameters of multiple cells. The validity of the new model is proven by comparison with measured S-parameters up to 40 GHz.

References

[1] Allam E A, Manku T. A small-signal MOSFET model for radio frequency IC applications [J]. *IEEE Transactions on Computer-Aided Design of Integrated Circuits and Systems*. 1997, **16**(5):437-447.
[2] GAO Jian-Jun, Werthof A. Direct parameter extraction method for deep submicrometer metal oxide semiconductor field effect transistor small signal equivalent circuit [J]. *IET Microwave, Antennas and Propagation*. 2009, **3**(4):564-571.
[3] Xu Jian-Fei, Yan Nan, Zeng X, Gao Jian-Jun. A 3.4 dB NF k-band LNA with a tapped capacitor matching network in 65 nm CMOS technology [J]. *International Journal of RF and Microwave Computer-Aided Engineering*. 2015, **25**(2):146-153.
[4] Eo Y, Eisenstadt W R. High-speed VLSI interconnect modeling based on S-parameter measurements [J]. *IEEE Transaction On Components, Hybrids, and Manufacturing Technology*. 1993, **16**(5):555-562.
[5] Kwon I, Je M, Lee K, *et al*. A simple and analytical parameter-extraction method of a microwave MOSFET [J]. *IEEE Transactions on Microwave Theory and Techniques*. 2002, **50**(6):1503-1509.
[6] Mei S, Ismail Y I. Modeling skin and proximity effects with reduced realizable RL circuits [J]. *IEEE Transaction on Very Large Scale Integration System*. 2004, **12**(4):437-447.
[7] Gao Jian-Jun, Werthof A. Scalable small-signal and noise modeling for deep-submicrometer MOSFETs [J]. *IEEE Transactions on Microwave Theory and Techniques*. 2009, **57**(4):737-744.